

Asphaltene precipitation under controlled mixing conditions in a microchamber

Jia Meng^a, Chiranjeevi Kanike^{a,b}, Somasekhara Goud Sontti^a, Arnab Atta^b, Xiaoli Tan^{a,*}, Xuehua Zhang^{a,**}

^a*Department of Chemical and Materials Engineering, University of Alberta, Alberta T6G 1H9, Canada*

^b*Department of Chemical Engineering, Indian Institute of Technology Kharagpur, Kharagpur, West Bengal 721302, India*

Abstract

Solvent exchange is a controlled process for dilution-induced phase separation. This work utilizes the solvent exchange method to reveal the effect of the mixing dynamics on the asphaltene precipitation process under 20 different mixing conditions using a model system of n-heptane and asphaltene in toluene. The external mixing between the asphaltene solution and the paraffinic solvent is strictly controlled. We employed high-spatial resolution total internal reflection fluorescence microscope to detect asphaltene precipitates with a resolution up to ~ 200 nm. A multiphysics model is used to simulate the evolution of oversaturation pulse in the solvent exchange process. Based on the simulation results, we predicted the effect of the flow rate, dimension, orientation of the microfluidic chamber, and temperature on the surface coverage and size distribution of asphaltene precipitates. The model predictions of all factors corroborate with the experimental observations. Local concentration of the solvent and shear forces are found to be the two main reasons for the change of asphaltene precipitation caused by mixing dynamics. However, the influence of thermodynamics is more critical than the mixing dynamics as temperature changes. Through a combination of experimental and simulation studies, this work illuminates the significance of the transportation process for the final morphology of asphaltene precipitates and provides a in-depth insight into the mechanism of mixing dynamics on the asphaltene precipitation. A smart mixing may be to boost new phase formation without excessive solvent consumption.

Keywords: Dilution-induced phase separation; Solvent exchange; Microfluidic chamber; Mixing dynamics; CFD

1. Introduction

Asphaltene plays an important role in energy sector through production, refinery, and transportant to value-added product from hydrocarbon-rich waste [1]. As a complex mixture containing polycyclic aromatic hydrocarbons, asphaltene is defined by solubility class that is soluble in aromatic solvents such as benzene and toluene and insoluble in n-alkanes solvents such as n-pentane and n-heptane [2]. On one hand, the presence of asphaltene hinders the coalescence of oil-water emulsions [3, 4], causing increase in operational cost and production challenges by forming flocculation and deposits in the reservoirs and transportation pipes. Undesirable asphaltene precipitation in the transportation pipes can cause severe problems such as clogging and blocking [5, 6]. On the other hand, dilution-induced asphaltene precipitation has been utilized in paraffinic froth treatment (PFT) units to remove impurities in bitumen such as water and solids. In this process, the particle size of asphaltene precipitates plays an important role, as they interact and agglomerate with water droplets and solid particles [7]. The precipitated asphaltene can be used as a raw material to make value-added products, such as absorbent, or carbon fibers [8–11]. Therefore, it is of importance to understand and control asphaltene precipitation.

Asphaltene is considered to form nano-aggregates and nano-clusters in a crude oil or aromatic solvents, unless at high dilution [12–16]. Asphaltene dispersed in toluene is more stable due to the balance of attractions (van der Waals, H-bonding, and acid base interactions) and steric repulsions originated from side alkane chains [17, 18]. Adding n-alkanes such as paraffinic solvents into the mixture of asphaltene and toluene leads to

*Corresponding author

**Corresponding author

Email addresses: xiaolit@ualberta.ca (Xiaoli Tan), xuehua.zhang@ualberta.ca (Xuehua Zhang)

the collapse of the side alkane chain layer and a reduction in steric repulsion. Consequently, asphaltene nano-aggregates grow to a larger size and manifest as precipitates or aggregates [19, 20]. The effective parameters that may affect asphaltene precipitation include temperature [21], pressure [22], addition of inhibitors [23], solvent to bitumen (S/B) ratio [24, 25], and type of the solvent [26].

Recently, the effect of mixing conditions on asphaltene precipitation has attracted the attention of researchers to understand aggregate formation [27–31]. In a conventional bulk system, when crude oil and paraffinic solvents were added into a container and mixed by a mixer, the resulting shear force caused by the agitation enhanced the growth rate of asphaltene particles, but the final size of the asphaltene particles was found to be smaller [27, 28]. The increase of the flow rate helped to increase the rate of deposition but the thickness of the final deposit layer was reduced [29–31].

The influence of mixing dynamics on asphaltene precipitation is mainly from two aspects. The impact of shear force on asphaltene aggregation and fragmentation [14, 32–34] and the variation in local compositions triggering asphaltene precipitation [35–38]. Extensive studies have been carried out to predict the deposition. However, there are knowledge gaps in the dynamics of dilution-induced asphaltene precipitation at the early stage. Importantly, the effects of local flow concentration and convection on asphaltene precipitation are challenging due to the poor mixing control. On the other side, the sampling procedures make it impossible to control convection. The results obtained from the direct visualization of asphaltene particles at a submicron scale may not be sufficient to investigate early-stage asphaltene precipitation due to the limited resolution of conventional optical microscopes. Microfluidic devices have been applied in the study of asphaltene precipitation with high reproducibility of results [39, 40]. For example, understanding the characteristics of the precipitates from mixing in confined spaces [41–43].

Solvent exchange, also called solvent shifting or solvent displacement has shown promising results in a quantitative understanding of solvent-induced phase separation

[44]. Controlled mixing by solvent exchange has led to fundamental insights into phase separation induced by dilution, including nanobubble and nanodroplet formation [45, 46], oiling out crystallization [47, 48], and polymer nanoprecipitation [49]. The approach of solvent exchange is displacing a solution in a good solvent with a poor solvent. Consequently, the new phase nucleates and grows at the mixing front due to a transient oversaturation [50]. The solvent exchange process is a well-controlled mixing system, which can be described by the advective diffusion equation [44]. Overall, the diffusive and convective mixing in the system is controllable by varying the dimension of the microfluidic chamber and the injection rate of the solvents. To the best of our knowledge, such fundamental studies on asphaltene precipitation are not yet reported in the open literature. In particular, the orientation and channel height of the chamber, the flow rate of the mixing, and the operating temperature can dictate the final morphology of asphaltene precipitates in terms of surface coverage (SC) and size distribution at the submicron and micron scales.

This research aims to understand the solvent-induced asphaltene precipitation under controlled convective mixing. The microfluidic flow rate, microchannel height, and orientation all enable the control of local concentration of the solvent and local shear force in the experiments. Systematic numerical investigations based on the finite element method (FEM) were performed to visualize the oversaturation pulse in the solvent exchange process for different geometric and flow conditions. Through the numerical results, we identified the generation of convective rolls when the channel height was more than a critical value due to gravity and buoyancy forces. Furthermore, the total internal reflection fluorescence microscope (TIRF) and optical microscope are used to resolve the asphaltene particles at the submicron and micron scales. In this work, the surface coverage (SC) is characterized to quantify the asphaltene yield. The size distribution at the submicron and micron scales is specified to investigate the aggregation of asphaltene particles. The implication is that the optimized flow condition may mediate the asphaltene precipitation without leveraging solvents. The findings of this work provide new insights

into the influence of mixing condition on asphaltene precipitation, and is not only applicable to asphaltene precipitation but also has implications for other dilution-induced phase separation processes.

2. Experimental section

2.1. Chemical and substrate preparation

Murphy Oil (USA) provided the C5-asphaltene (i.e., n-pentane precipitated asphaltene) used in this project. The analysis of elementary and the pre-treated method of the asphaltene sample can be found in our previous research [51]. In brief, raw asphaltene sample was dissolved in toluene (Fisher Scientific, ACS grade, 99.9 %+) to remove any inorganic solvents by 0.22 μm polyvinylidene difluoride (PVDF) filter paper. A rotary evaporator was then used to remove toluene from the inorganic solid free asphaltene. 17 g of inorganic solid-free asphaltene sample was dissolved in toluene to make 1 L of asphaltene in toluene solution (i.e., solution A). The results of diluted crude oil are similar to that of asphaltene in toluene solution at early stage of asphaltene precipitation [43]. n-Heptane (Fisher Chemical, 99%) was used as the solvent (i.e., solution B) for asphaltene precipitation.

A high-precision cover glass (Azer Scientific) was used as the substrate. Before the experiment, the cover glass was sonicated in toluene for 5 min and dried by air to remove any contaminates.

2.2. Solvent exchange process

The solvent exchange process was performed in a custom-built microchamber. The experiments were performed at ambient pressure, as the current design of microfluidic chamber did not allow for varying the pressure. The apparatus is shown in Figure 1(a). The micro-channel was 35 mm long and 5 mm wide. Glass was used as a top wall and a spacer in between the glass and substrate was used to seal the system. The channel height was adjusted by using spacers of different thickness.

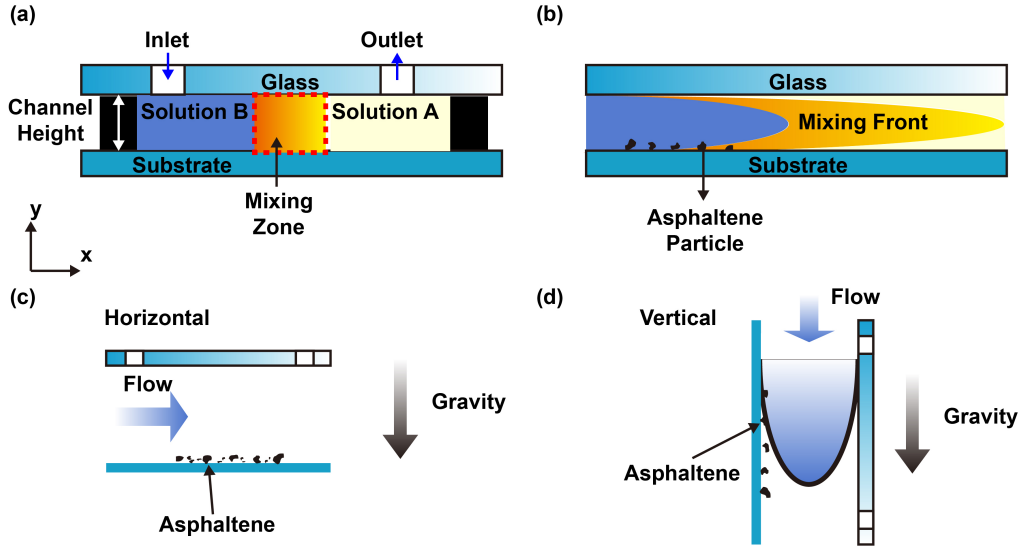


Figure 1. (a) Sketch of the microchamber used in this study. (b) Zoomed-in image of the mixing front in (a). The flow direction is along the x-axis. The microchamber is placed (c) horizontally, (d) vertically to examine the effect of orientation.

The model oil (solution A) was first injected into the microchamber using a syringe pump (NE-1000, Pumpsystems Inc.). Afterwards, n-heptane (solution B) was injected into the device to displace solution A, creating a mixing front between solution A and solution B as shown in Figure 1(b). The asphaltene precipitation began at the moment when the concentration of n-heptane is higher than the onset point in the mixing front. At the moment, the solution A was completely displaced by solution B, asphaltene precipitation stopped due to lack of dissolved asphaltene. After injecting 2.5 mL of solution B (i.e., at least ten times the total volume of solution A), the asphaltene precipitation was considered the final state. Air was injected into the chamber to drive away from the remaining liquid. After the solvent exchange process, the liquid was removed with a 5 mm/s of a constant air flow velocity, in all of the experimental conditions. Subsequently, the substrate was examined by the microscopes. The microchamber was placed both horizontally (Figure 1(c)) and vertically (Figure 1(d)) to examine the gravitational

effect.

2.3. Effect of flow rate, channel height, orientation, and temperature

This work investigated the influence of four aspects on asphaltene precipitation that include injection flow rate of solution B, channel height, orientation of the microfluidic chamber, and temperature. A horizontally placed 1,000 μm height microfluidic chamber was used to study the influence of flow rate under the ambient condition (i.e., 19 - 21°C, 1 atm). The flow rate of solution B was varied from 15 mL/h to 150 mL/h. The Reynolds number (Re) and Péclet number (Pe) were calculated from $Re = \frac{Q}{wv}$ and $Pe = \frac{Q}{wD}$, respectively [44], where Q , w , v , D are the microfluidic flow rate, width of the microchamber, kinematic viscosity, and diffusion coefficient, respectively. Table 1 summarizes the flow rate and the corresponding Re and Pe .

Table 1. Flow rate and the corresponding Reynolds number and Péclet number in the experiments.

Flow Rate (mL/h)	Reynolds Number	Péclet Number
15	1.37	458
30	2.73	916
60	5.47	1,832
90	8.20	2,747
120	10.94	3,663
150	13.67	4,579

Seven spacers of different thickness from 90 μm to 1,000 μm were used to investigate the effect of channel height. The buoyancy and gravity effects of different channel heights can be estimated by a dimensionless number, Rayleigh number (Ra), as shown in Equation (1) [44]. Table 2 showed the corresponding Rayleigh number of each channel height.

$$Ra = \frac{\Delta\rho g(h/2)^3}{\mu D} \quad (1)$$

where $\Delta\rho$ is the density difference between solution A and solution B, g is the gravita-

tional constant, h is the channel height, μ is the viscosity of solution B, and D is the diffusion coefficient.

Table 2. Channel height and the corresponding Rayleigh number in the experiments.

Channel Height (μm)	Rayleigh Number
90	219
180	1,753
260	5,283
340	11,814
430	23,899
510	39,873

To study the influence of chamber orientation, the device filled with solution A was placed horizontally and vertically (Figure 1(c)-(d)). Solution B was then injected at 30 mL/h . Four elevated temperatures of 35 °C, 50 °C, 58 °C, and 65 °C were compared with the results of the ambient temperature. The densities, diffusion coefficients and viscosities at those temperatures are listed in Table ???. All the solutions were immersed in the water bath for 30 *min* before conducting the experiments to attain thermal equilibrium. The entire solvent exchange system, including the horizontally placed microchamber and pipes, were immersed into the water bath to keep the temperature constant during the experiments. The channel height was kept 1,000 μm and the flow rate of solution B maintained a constant flow rate of 90 mL/h for all the elevated temperatures.

2.4. Observation and characterization of the asphaltene precipitates

Total internal reflection fluorescence (TIRF) mode of a confocal microscope (Leica TCS SP8) was used to capture high-resolution images. A 488 nm laser was used to excite the fluorophores of asphaltene. The spatial resolution was $\sim 200 nm$ to show the details of asphaltene particles at the submicron scale. An optical microscope (Nikon ECLIPSE Ni) equipped with Nikon DS-FI3 camera was used to detect asphaltene particles at the micron scale. MATLAB (The MathWorks, Inc., US) and ImageJ (open source software) were used to analyze the images. The details of the process for image analysis can be found in our previous work [42, 51]. In brief, the main steps were to transform the

microscopy images into binary images and then to obtain the information of particles such as perimeter and area. The particle size distribution smaller than one micron was obtained from the TIRF images, while the surface coverage and particle size distribution larger than one micron were obtained from the optical microscope images.

2.5. Description of the numerical model

In the present study, Level-Set (LS) method is coupled with the Transport of Diluted Species (TDS) physics adopted to track the interface between the two fluids and the concentration of the dissolved species at the oversaturation region.

2.5.1. Transport of diluted species

The transport of diluted species model solves the chemical species transport through diffusion and convection. This method resolves the mass conservation equation for oversaturation pulse, which can be written as:

$$\frac{\partial C_i}{\partial t} + \nabla \cdot J_i + \vec{U} \cdot \nabla C_i = 0 \quad (2)$$

where C_i , D_i , \vec{U} , and J_i are the concentration of species, diffusion coefficient, mass average velocity vector, and mass diffusive flux vector, respectively. The mass flux J_i is further defined as $J_i = -D_i \nabla C_i$.

2.5.2. Level-Set model

A conservative level-set method [52] was combined with the transport of diluted species model to visualize the effect of gravity. In addition to the aforementioned equation for transport of diluted species, a set of coupled governing equations consisting continuity, momentum (incompressible Navier-Stokes equation), and a level-set equation was solved.

Equation of continuity:

$$\nabla \cdot \vec{U} = 0 \quad (3)$$

Equation of motion:

$$\rho \frac{\partial(\vec{U})}{\partial t} + \rho \nabla \cdot (\vec{U} \vec{U}) = -\nabla P + \nabla \cdot \mu (\nabla \vec{U} + \nabla \vec{U}^T) + \rho g + \vec{F}_{SF} \quad (4)$$

where \vec{U} , ρ , μ , P , and \vec{F}_{SF} are velocity, density, dynamic viscosity of fluid, pressure, and interfacial tension force, respectively.

Equation of Level-Set (LS) Function:

The interface in a level-set method is captured by a conservative level set method (CLSM). The level function changes smoothly across the interface from 0 to 1, when $\phi = 0$, it indicates one fluid domain and $\phi = 1$ in another fluid domain. The smooth interface between the phases is defined by the 0.5 isocontour of ϕ . The following equation describes the convection of the reinitialized level set function [53].

$$\frac{\partial \phi}{\partial t} + \mathbf{u} \cdot \nabla \phi = \gamma \nabla \cdot \left(\epsilon \nabla \phi - \phi(1 - \phi) \frac{\nabla \phi}{|\nabla \phi|} \right) \quad (5)$$

where ϵ is a parameter to determine the thickness of the transition layer where ϕ goes smoothly from zero to one. It is typically of the same order as the size of the elements of the mesh. The parameter γ determines the amount of reinitialization or stabilization of level set function [54]. The coupling of transport of diluted species interface with the level-set physics adds an additional transport equation for computing the concentration of dissolved species ‘‘C’’. The convective transport of ‘‘C’’ is based on the velocity field from the two-phase flow, level-set physics.

2.5.3. Computational parameters, implementation and model validation

Systematic numerical investigations were performed to understand the mixing condition during solvent exchange process inside the microchamber. Two-dimensional transient simulations were carried out using a finite element method based solver COMSOL Multiphysics V. 6.0. (COMSOL AB, Stockholm, Sweden). Asphaltene dissolved in

toluene was considered as fluid-1 and n-heptane (solvent for asphaltene precipitation) was considered as fluid-2 in the computational domain. All the details of the fluid properties (i.e., density and viscosity) corresponding to experimental conditions are provided in the supporting information in Table S1. For different temperature conditions, toluene and n-heptane properties were estimated using UNIFAC thermodynamic model with the software package Symmetry [55]. Influence of different microchannel geometries (i.e., height, see Table 2) and various flow rates (see Table 1) were examined. Unsteady state diffusion equation coupled with the velocity field was solved to obtain the evolution of the mixing front with space and time [56]. The velocity inlet boundary condition was applied to the microchannel inlet, and the pressure outlet boundary condition was used at the outlet as shown in Figure 2(a).

Table 3. Meshes in the grid independence study

Grid	Total number of elements	Number of boundary elements	Maximum element size (mm)	Average mesh quality (skewness)	Difference (%) w.r.t G7
G1	3,500	730	0.10000	1.0	4.06
G2	6,552	978	0.0750	1.0	2.81
G3	14,000	1,460	0.0500	1.0	1.76
G4	25,218	1,949	0.0375	1.0	1.34
G5	35,008	2,248	0.0320	1.0	0.95
G6	56,000	2,920	0.0250	1.0	0.51
G7	224,000	5,840	0.0125	1.0	-

No-slip boundary condition was imposed at the top and bottom walls and inflow with zero concentration at the inlet. At $t = 0$, the oversaturation pulse in a narrow region (i.e., $100 \mu m$ thick) was initialized vertically along the inlet with a uniform concentration. The oversaturation pulse was convected and diffused simultaneously inside the microchannel, once the flow is initialized. The computational domain was meshed with quadrilateral mesh elements (Figure 2(b)). Grid independence study was initially performed using different element sizes ranging from 0.10 to 0.0125 mm . Mesh quality and number of elements details are reported in Table 3. The velocity profiles were compared for different meshes as shown in Figure 2(c), and an optimum mesh element size of 0.025 mm was

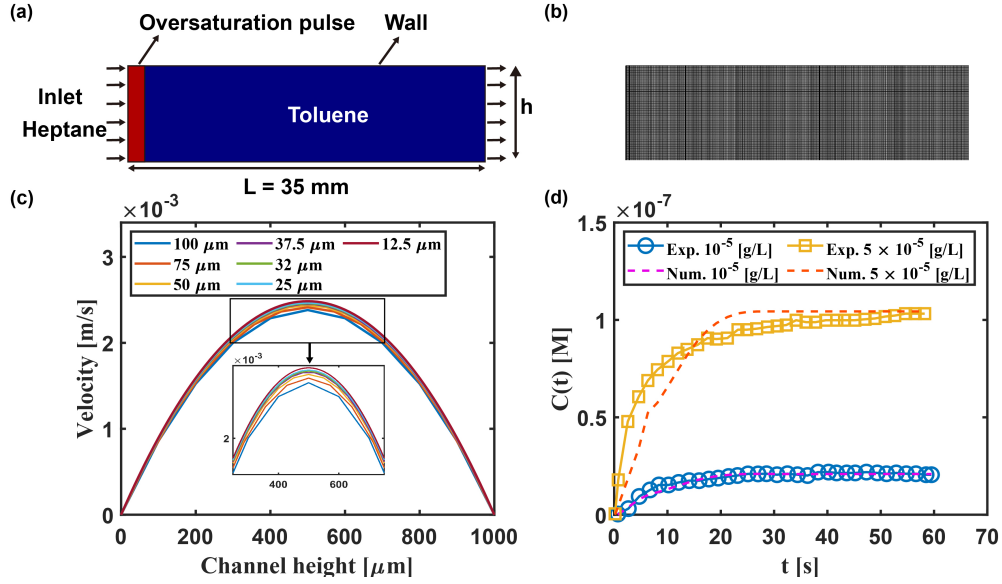


Figure 2. (a) 2D schematic representation of the computational domain with imposed boundary conditions, and (b) computational grid. (c) Influence of grid numbers on the inlet velocity profiles along the height of the channel. (d) Model Validation with the experimental results reported in our previous work [57]. Blue circles and yellow squares represent the experimental data. Pink and red dashed lines represent the numerical results from our model for the same system.

considered for the numerical investigations. Different sets of simulations were performed in a high performance computing (HPC) facility for the same flow conditions (Pe , Ra , Re , h , and Q) as used in the experiments. For each simulation, 48 CPUs were used to run the 30 s of flow time.

At first, the developed CFD model was validated with the relevant experimental data from our previous study [57]. The length, width and the height of the considered microchamber are 45 mm, 13 mm, and 0.3 mm respectively, which are within the range of our current microchamber dimensions. The flow rate at the inlet was set to 50 mL/h and other fluid properties were kept similar to our previous study [57]. Figure 2(d) shows a comparison of the analyte concentration as a function of time. The CFD model

predictions were found to be in good agreement with experimental data. Therefore, the developed CFD model was capable to predicted underlying phenomena of solvent exchange process.

3. Results and Discussion

In the solvent exchange process, solution B gradually displaces solution A. Simultaneously, asphaltene from solution A diffuses to solution B, and n-heptane diffuses towards solution A. As the diffusion process advances, The S/B ratio in the mixing zone gradually increases beyond the onset, until the concentration of asphaltene in the mixing front is oversaturated. At $t = 0$, the asphaltene in solution A is undersaturated. As time progresses, the asphaltene becomes oversaturated in the mixing region, which triggers the formation of asphaltene precipitate. Once the solution A is completely displaced by the solution B, the formation of asphaltene precipitate stops due to lack of asphaltene. The duration of the oversaturation pulse is independent of the flow velocity due to the no-slip boundary and depends on the diffusion of chemicals from the mixing front to the substrate [44]. Therefore, the new phase formation on the substrate is determined by the profile of the mixing front.

3.1. Effect of the flow rate

Simulation results show the oversaturation pulse profile for different flow rates in Figure 3. The non-blue area is the mixing front, and the color scale bar indicates the corresponding concentration of oversaturation pulse in the system. At Pe of 458, the oversaturation pulse passes through the entire chamber in 16 s. At the highest Pe of 4,578, the duration of the pulse is approximately 2.7 s. Although the time for the precipitation is considerably shorter at larger Pe , the oversaturation levels near the bottom wall are similar through the entire process at all Pe , as exhibited by the consistent blue zone at the bottom in all snapshots. Therefore, diffusion of asphaltene and n-heptane towards the substrate at different Pe should be comparable because the concentration

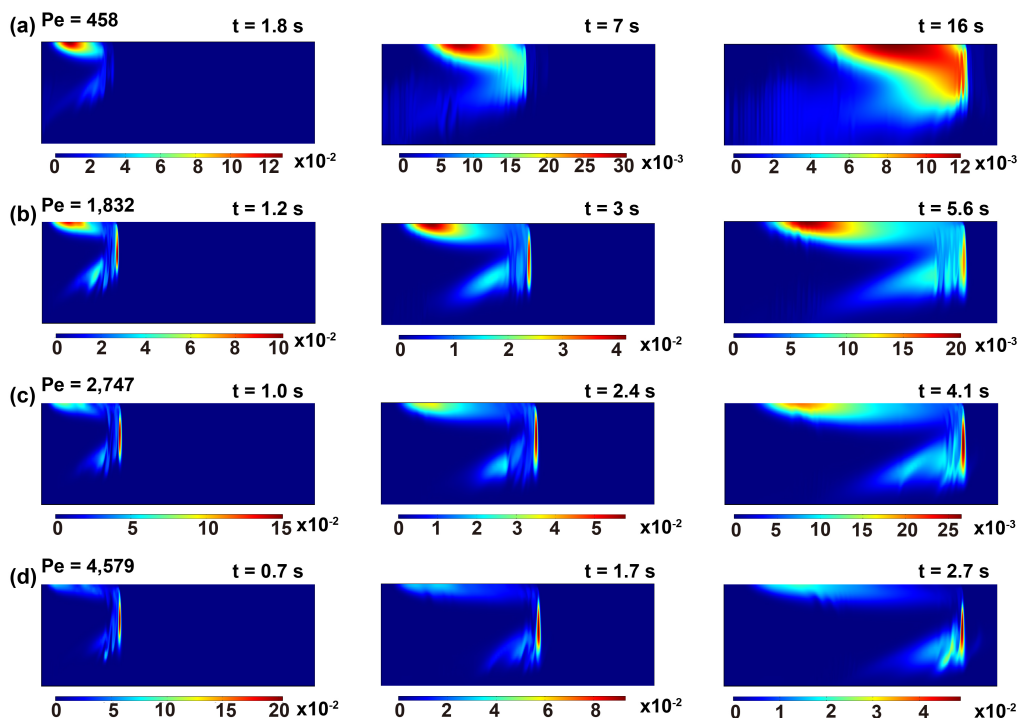


Figure 3. COMSOL simulation for the profile of the oversaturation pulse at (a) $Pe = 458$, (b) $Pe = 1,832$, (c) $Pe = 2,747$, and (d) $Pe = 4,579$.

gradient is identical, resulting in a similar SC of asphaltene on the bottom wall. At any given moment, the level of the oversaturation on the top plate is substantially higher at lower Pe , which may lead to more precipitates on the top surface.

Figure 4(a) shows the optical images of asphaltene precipitation in the solvent exchange with the flow rate of solution B ranging from 15 mL/h to 150 mL/h (i.e., Pe from 458 to 4,579). The black dots are asphaltene particles formed on the substrate placed on the bottom wall. It is worth mentioning that only the area with asphaltene particles is considered. The areas of asphaltene layers, as shown in Figure ??(b), are omitted when analyzing surface coverage (SC) and the size distribution of asphaltene particles because these large deposits may be agglomerates formed in the bulk. Figure 4(b) shows SC of the asphaltene particles divided by the total area, which is approximately independent

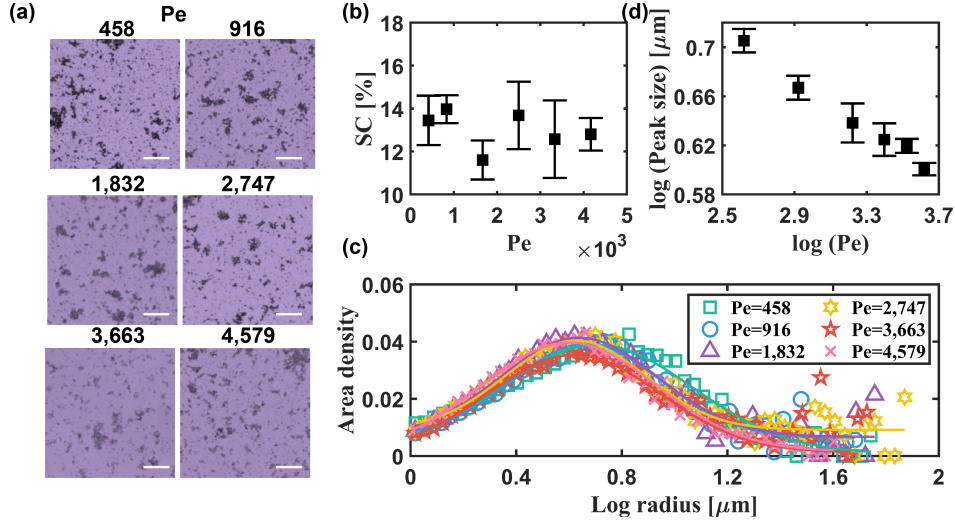


Figure 4. (a) Optical images of asphaltene particle at the final state of different Péclet numbers. The length of the scale bar is $20 \mu\text{m}$. The images are false-colored. (b) SC of asphaltene particles at the final state as a function of Péclet number. (c) Size distribution of asphaltene particles for different Pe . The solid lines are the Gaussian fitting for the results. (d) The corresponding peak size of Gaussian fitting of (c) vs. Péclet number.

of Pe and is always $\sim 14\%$.

Figure 4(c) shows the size distribution of asphaltene particles. The distribution is plotted based on area density instead of the number density [58] to compare with the conventional study in a bulk system. Interestingly, the Gaussian distribution can fit the area density-based size distribution for each Pe . This Gaussian distribution is consistent with the presented results in a conventional mixing system [58]. The peaks of the size distribution in Figure 4(c) shift to the left with the increase of Pe , indicating the size of asphaltene particles decreases with the increase of Pe (Figure 4(d)).

Figure 5(a) shows the TIRF images of asphaltene particles at different Pe . The white speckles are the asphaltene particles due to the natural fluorescence property of asphaltene under 488 nm laser excitation in air. Number density-based relative frequency is introduced to analyze the size distribution quantitatively. The relative frequency of

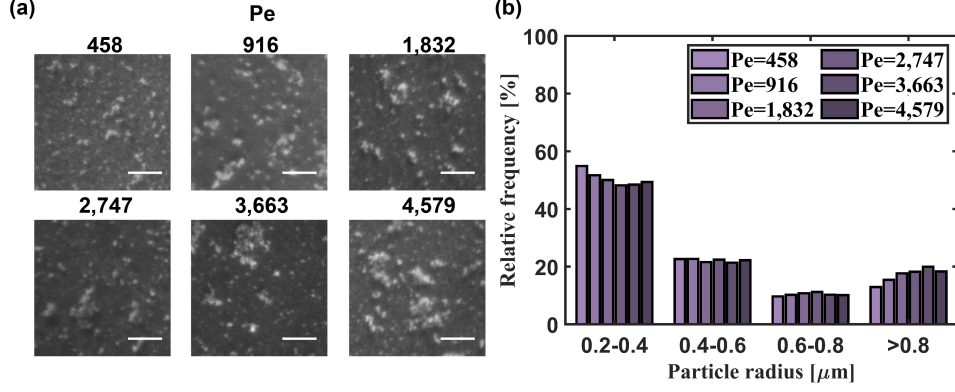


Figure 5. (a) TIRF images of asphaltene particles at the final state of different Pe . The length of the scale bar is $5 \mu m$. (b) Relative frequency of size distribution of asphaltene particles at different flow rates.

each size bin is calculated by the number of particles of the corresponding size divided by the total number of particles. For primary submicron particles (PSMPs), which are defined as the radius from 200 to 400 nm [41], the relative frequency denotes the degree of aggregation at the early stage. A high relative frequency of PSMPs (R_p) represents the low possibility of PSMPs aggregating into larger particles after the precipitation. From the quantitative examination, as shown in Figure 5(b), it can be observed that R_p decreases with the increase of Pe . R_p is calculated by:

$$R_p = \frac{N_{psmp}}{N_{psmp} + N_{smp}} \quad (6)$$

where N_{psmp} and N_{smp} are the quantity of primary submicron particles and quantity of submicron particles, respectively.

Interestingly, the size of asphaltene particles correlates with the flow rate because of the mass transfer process of asphaltene from the oversaturation pulse to the substrate. The size of asphaltene particles decreases with Pe at micron-scale (Figure 4(c)) but increases at submicron scale (Figure 5(b)). The particle aggregation and fragmentation process are discussed to examine the reasons for the opposite trend of size distribution

at submicron and micron scales. Based on the Smoluchowshi aggregation model, the aggregation is:

$$\frac{dn_k}{dt} = \frac{1}{2} \sum_{i+j=k} K_{i,j} n_i n_j - n_k \sum_{i \geq 1} K_{i,k} n_i \quad (7)$$

where n_i , n_j , and n_k is the number density change of particle of size i , j , and k , respectively. t is time, and $K_{i,j}$ is aggregation kernel, which is calculated by $K_{i,j} = \alpha_{i,j} \beta_{i,j}$, where $\alpha_{i,j}$ is the collision frequency and $\beta_{i,j}$ is the collision efficiency of particles. $\beta_{i,j}$ is:

$$\beta_{i,j} \propto \exp\left[-\frac{1}{k_B T (\delta_{asp} - \delta_{sol})^2}\right] \quad (8)$$

where k_B is Boltzmann constant, δ_{asp} and δ_{sol} are Hildebrand solubility parameters of asphaltene and the paraffinic solvent, respectively. $\alpha_{i,j}$ is driven by two factors in our system, including Brownian motion and shear force [27, 28, 59–61]:

$$\alpha_{i,j} = \frac{2}{3} \frac{RT}{\mu} \frac{(d_i + d_j)^2}{d_i d_j} + \frac{G}{6} (d_i + d_j)^3 \quad (9)$$

where R is the ideal gas constant. T is temperature. μ is viscosity. d_i , and d_j are the diameters of particles with sizes i and j , respectively, G is the shear rate.

The oversaturation level near the bottom wall is similar for all the Pe (Figure 3). Regardless, the velocity gradient between the maximum point of the flow and the minimum point adjacent to the substrate increases with Pe . The increased shear force leads to the increase of aggregation of PSMPs at an early stage (Equation (9)), ultimately resulting in lowering of R_p (Figure 5(b)).

However, shear force brings an increase in the aggregation and the fragmentation of aggregates. The mechanism of fragmentation induced by shear rate is due to different pressures gradient on the opposite sides of the aggregates [62]. The fragmentation rate (B_i) increases with the particle volume (V_i) and the shear rate ($B_i = kG^y V_i^{1/3}$), where k is a proportionality fitting constant, y is a constant inversely proportional to the interac-

tion strength between particles [27, 63–65]. Therefore, when the asphaltene particles are large enough (i.e., at the micron scale), the fragmentation yielded by shear force prevails, resulting in the decrease of particle size with the increase of shear rate (Figure 4(d)). It is worth noting that there is no maximum critical size for the asphaltene particles in the solvent exchange process because the chemical composition varies with time.

3.2. Effect of the microchamber height

A dimensionless number (Rayleigh number, Ra) is used to quantitatively analyze the impact of channel height on SC (Table 2). The oversaturation levels near the bottom wall are always high, as exhibited by the red color in Figure 6. At Ra of 219, the oversaturation pulse passes through the chamber in 2.1 s. At the highest Ra of 39,873, the duration of the pulse is approximately 9.3 s. The increased duration of the oversaturation pulse provides a longer time for asphaltene precipitation and aggregation. Therefore, mass transfer of asphaltene from the oversaturation pulse to the substrate should increase with the increase of the Ra , resulting in a higher SC and larger size of asphaltene particles.

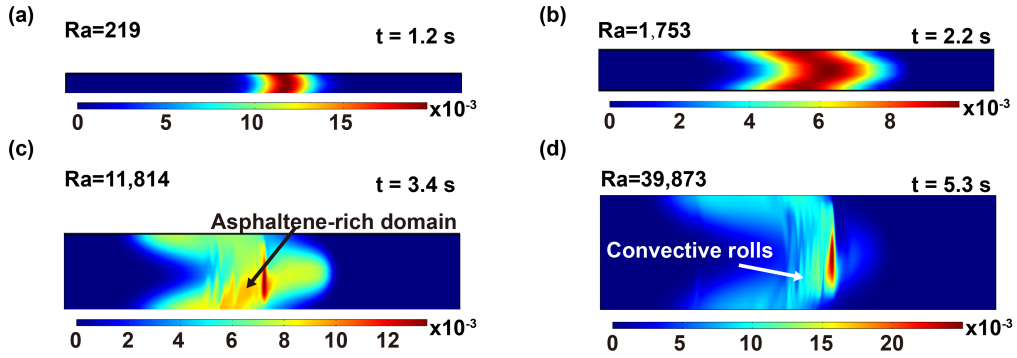


Figure 6. COMSOL simulation for the profile of the oversaturation pulse at (a) $Ra = 219$, (b) $Ra = 1,753$, (c) $Ra = 11,814$, and (d) $Ra = 39,873$.

Figure 7(a) shows the optical microscope images of asphaltene precipitates in channel heights from 90 μm to 510 μm under the same Pe . It is found that more asphaltene particles are formed with the increase of the channel height. Meanwhile, the size of

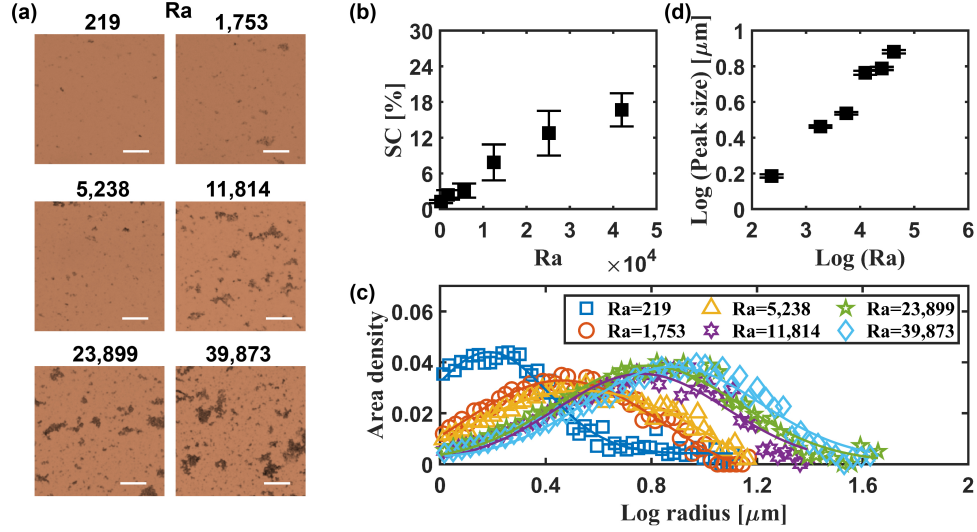


Figure 7. (a) Optical images of asphaltene particles at the final state for different Ra . The length of the scale bar is $20 \mu\text{m}$. The images are false-colored. (b) SC of asphaltene at the final state as a function of Rayleigh number. (c) Size distribution of asphaltene particles for different channel heights. The scatters are the experimental data and the solid lines are the Gaussian fitting for the results. (d) The corresponding peak size of Gaussian fitting of (c) vs. channel height.

asphaltene particles increases with the increase of the channel height. SC increases with Ra (Figure 7(b)). The relationship is almost linear. However, the linear relationship is not held when the channel height is $1,000 \mu\text{m}$ as shown in Figure ??(a). At $1,000 \mu\text{m}$, many asphaltene deposits do not exist as particles but form a layer of sediments, as shown in Figure ??(b). Therefore, SC increases as the channel height increases and eventually reaches a maximum value. The formation of a larger SC and a layer of sediments of asphaltene are in line with the numerical findings. Figure 7(c) shows the size distribution of asphaltene particles as a function of Ra . The size distribution for each Ra can be fitted by Gaussian distribution. The Gaussian curve peaks increased from ~ 0.2 to ~ 0.9 with Ra increasing from 219 to 39,873. It indicates that the mean particle radius increases from $1.6 \mu\text{m}$ to $7.9 \mu\text{m}$ as shown in Figure 7(d). Particle size

increases with Ra because better solution mixing leads to an increase in particle collision efficiency β in Equation (8), resulting in larger particles. These observations are also consistent with our numerical model predictions.

Our simulations for the vertically placed devices also demonstrate that the duration of the oversaturation pulse increases with the increase of the channel height, as shown in Figure 8(d), which is consistent with the horizontally placed devices. Therefore, the SC increases with the channel height and the size distribution shifts to the right with the increase of channel height (Figure 8(a)-(c)).

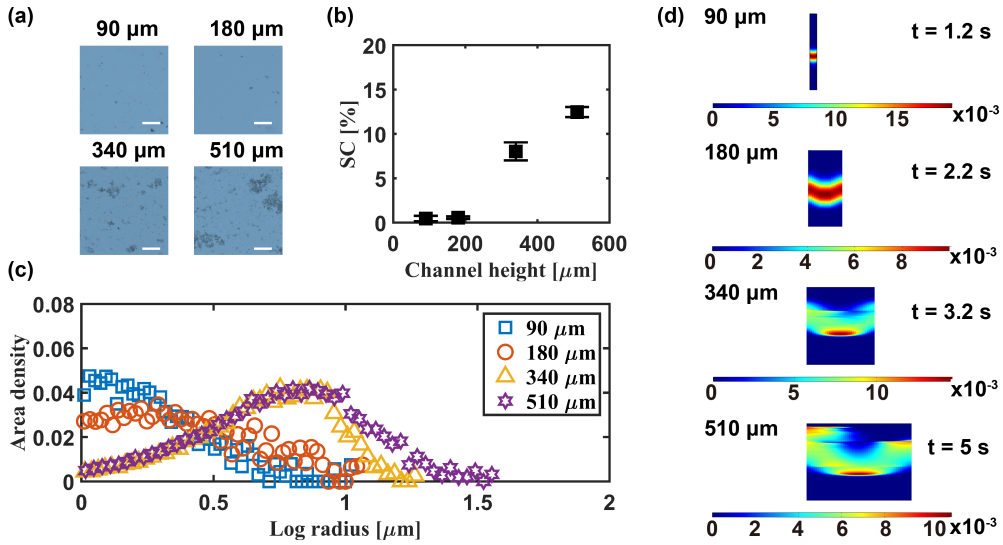


Figure 8. (a) Optical images of asphaltene particles at the final state of different channel heights. The length of the scale bar is $20 \mu m$. The images are false-colored. (b) Surface coverage of asphaltene at the final state as a function of channel heights. (c) Size distribution of asphaltene particles for different temperatures. The solid lines are the Gaussian fitting for the results. (d) COMSOL simulation for the profile of the oversaturation pulse at different channel heights.

TIRF images of the final state of asphaltene particles are captured to show the details of asphaltene particles at the submicron scale, and is shown in Figure 9(a). It can be seen from Figure 9(b) that R_p decreases from $\sim 65\%$ to $\sim 52\%$ with the increase of

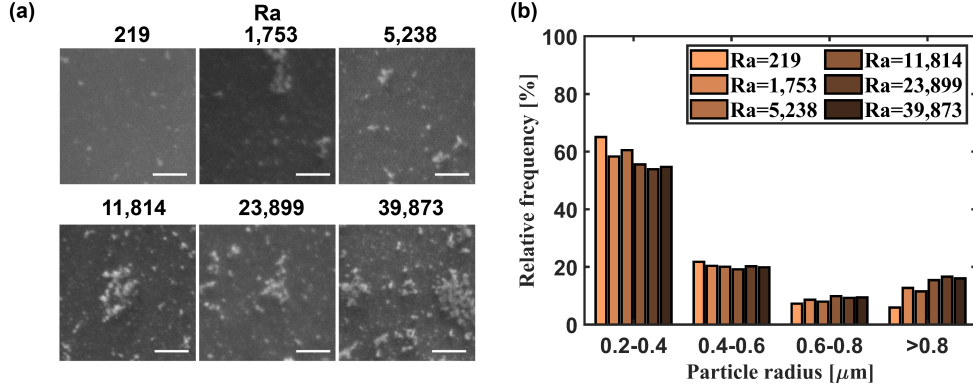


Figure 9. (a) TIRF images of asphaltene particles at the final state for different channel heights. The length of the scale bar is $5 \mu m$. (b) Relative frequency of the size distribution of asphaltene particles of different channel height.

Ra from 219 to 39,873, reflecting the aggregation of particles is more intensified in the channel with a more significant height. Correspondingly, the proportion of large particles, especially those larger than $0.8 \mu m$, increases with the increase of the channel height. This observation at the submicron scale is consistent with that at the micron scale.

3.3. Effect of the microchamber orientation

In the device with the same channel height, the oversaturation pulse takes the same time to pass through the channel in both horizontal and vertical devices. However, the mixing dynamics are different. When the channel height is $510 \mu m$ (Ra is 39,873 for the horizontally placed device), simulation results showed the formation of convective rolls (Figure 6(d)) in the horizontally placed device, leading to better mixing between solutions A and B. The final maximum oversaturation level for the horizontally placed device is approximately 0.02, while the one for the vertically placed device is approximately 0.01. In addition, the oversaturation area is not in the middle but shifts downwards and thus closer to the bottom wall because the asphaltene is heavier compared with n-heptane and toluene, an asphaltene-rich domain forms at the tail of the profile of the oversaturation pulse (Figure 6(c)). However, the asphaltene-rich domain does not appear

in the vertically placed cases. The loss of convective rolls and asphaltene-rich domain in the vertically placed devices results in reduced mass transfer compared to horizontally placed devices. Therefore, diffusion of asphaltene and n-heptane towards the substrate of the vertically placed device should be smaller than the horizontally placed device, resulting in the decrease of SC and left-shift of the particle size distribution.

Figure ??(a) shows the comparison of optical images of asphaltene precipitates between horizontally and vertically placed devices. The horizontally placed device has a higher SC of asphaltene particles than the vertically placed device, especially for $510\ \mu m$ (Figure ??(b)). SC increases from $\sim 12\%$ to $\sim 18\%$, revealing more asphaltene deposits on the substrate, which is in line with the numerical results.

The numerical results of varying Péclet number displays stack-like extreme convective rolls and very large asphaltene-rich region (Figure ??). Video S1 (see supplementary information) shows a backflow after the mixing front reaches the outlet. Therefore, the SC may increase sharply when the channel height is $1,000\ \mu m$. The formation of the layer of sediments in the $1,000\ \mu m$ channel height group is consistent with our numerical results in Figure ??(b). Due to the intense mixing of the model oil and solvents, the asphaltene precipitation at $1,000\ \mu m$ may be closer to that in the bulk phase mixing system in the conventional study [66].

Orientation direction can also affect the size distribution of the asphaltene particles deposited on the substrate. Figure ??(d)-(f) reveals the rightwards shift of particle size in the horizontally placed device, meaning the asphaltene particles are relatively large in horizontally placed devices compared with the vertically placed ones. However, the shift of size distribution is not observed in the $90\ \mu m$ microchamber (Figure ??(c)). This is due to Ra is smaller than the critical value (1,708) when the channel height is $90\ \mu m$ [44]. The convective rolls and asphaltene-rich domain are not observed in the horizontally placed device.

In the solvent exchange process, particles may form on the substrate and in the bulk of the liquid simultaneously. The particles formed in the bulk may settle down onto

the substrate under gravity in the horizontally placed device. This is mainly due to the competition between gravity and Brownian motion. Brownian motion of the particles ($\overline{X}_{Brownian}$) is [67]:

$$\overline{X}_{Brownian}^2 = \frac{4RTK_m t}{3\pi^2\mu Nd} \quad (10)$$

where R is the ideal gas constant, T is temperature, K_m is the correction for discontinuity of fluid, which is 1 for liquid. t is time, which is calculated by dividing the volume of the microchamber by the flow rate, μ is the viscosity of the solvent, N is Avogadro constant, d is the diameter of particles. The Stokes settling motion of a particle is [67]:

$$\overline{X}_{Settling} = \frac{(\rho_{asp} - \rho_{sol})gd^2t}{18\mu} \quad (11)$$

where ρ_{asp} is the density of asphaltene and ρ_{sol} is the density of the solvent. For each channel height, only the particles with a diameter larger than $8 \mu m$ (logarithmic radius is 0.6) can settle under gravity. However, the rightwards shift is observed of particles smaller than $8 \mu m$ as shown in Figure ??(d). In addition, particles larger than $8 \mu m$ in Figure ??(c) of $90 \mu m$ device do not show a rightwards shift. Therefore, gravity-induced settlement is not the reason for the rightwards shift in horizontally placed devices. The increase of particle size is also due to the enhancement of solution mixing in the horizontally placed device.

3.4. Effect of the temperature

The density difference between solutions A and B does not change significantly with the change in temperature (Table ??). The duration for the oversaturation pulse to completely pass the entire channel is approximately $4 s$ for all the examined temperatures. Figure 10 shows the profile of the oversaturation pulse near the bottom wall does not change much with the increase in temperature, as indicated by the consistent blue zone. In addition, from the experiments performed in the $1,000 \mu m$ microchamber, it was evident that there was sufficient mixing in all of the temperatures due to the presence

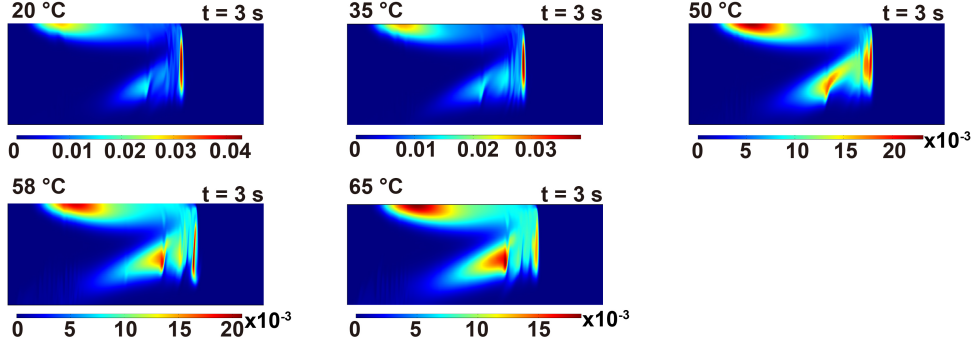


Figure 10. COMSOL simulation results of the oversaturation profile at 20 °C, 35 °C, 50 °C, 58 °C, and 65 °C.

of convective rolls, as shown in Figure ???. Therefore, mixing at all the temperatures we studied should be adequate.

Figure 11(a) shows the optical images of asphaltene particles at different temperatures. SC from 20 °C to 58 °C are similar but SC of 65 °C is much smaller than the other groups. The size distribution shows a rightwards shift trend with the increase of temperature from 20 to 58 °C. But the size distribution shifts to left from 58 to 65 °C (Figure 11(b)-(d)). The experiment results are mainly due to the thermodynamics influence. Asphaltene is a mixture of different fractions, and the increase in temperature resulted in some asphaltene fractions becoming soluble in asphaltene [68]. The reason may be the increase of steric repulsion between asphaltene particles caused by the increase in temperature [19, 20]. These asphaltene fractions do not precipitate, resulting in a decrease of SC at 65 °C. This observation is consistent with the previous study in a conventional bulk system [66].

Figure 12(a) shows the TIRF images of asphaltene particles. The quantitative size distribution at the submicron scale is shown in Figure 12(b). In summary, PSMPs are less likely to aggregate into fractal particles with increasing temperature.

Equations (8) and (9) show both the collision frequency and efficiency increase with temperature. Therefore, the overall right-shift trend from 20 °C to 58 °C in micron

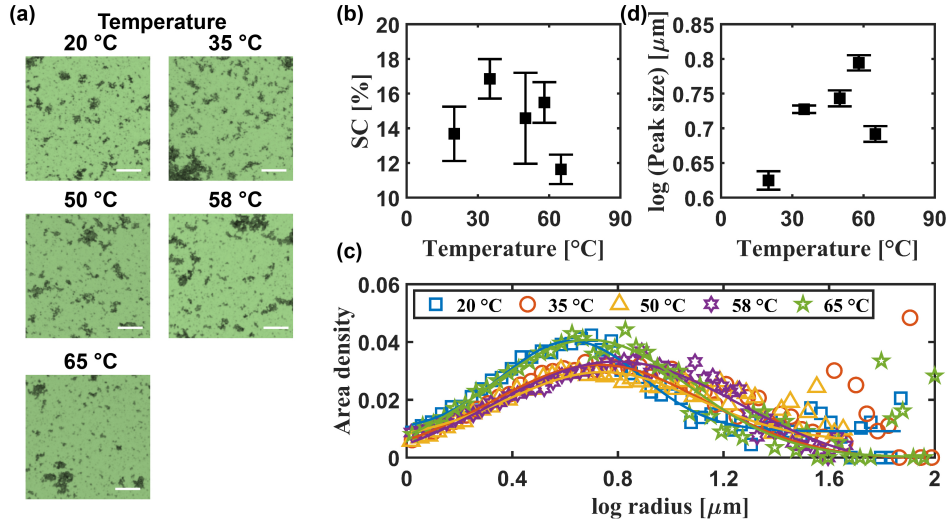


Figure 11. (a) Optical images of asphaltene particles at the final state of different temperatures. The length of the scale bar is 20 μm . The images are false-colored. (b) Surface coverage of asphaltene at the final state as a function of temperature. (c) Size distribution of asphaltene particles for different temperatures. The solid lines are the Gaussian fitting for the results. (d) The corresponding peak size of Gaussian fitting of (c) vs. temperature.

scale is expected in Figure 11(c) and (d). The leftwards shift from 58 °C to 65 °C is caused by asphaltene dissolution in n-heptane at 65 °C, as we discussed in the previous section. However, it is surprising that R_p increases apparently from $\sim 48\%$ to $\sim 58\%$ with the increase of temperature at the submicron scale (Figure 12(b)). In this regard, it is to be noted that asphaltene is a mixture of several fractions. The responses of various fractions to temperature are different [69]. The increase in temperature causes some fractions of asphaltene become more soluble in n-heptane. The Hildebrand solubility parameter difference in Equation (8) is lower. The repulsive interaction between this 'soluble-like' fraction of asphaltene particles is high when they form PSMPs, causing a decrease in collision efficiency for further aggregation. In addition, a decrease in SC also leads to less possibility of PSMPs aggregation [43]. As a result, the PSMPs formed

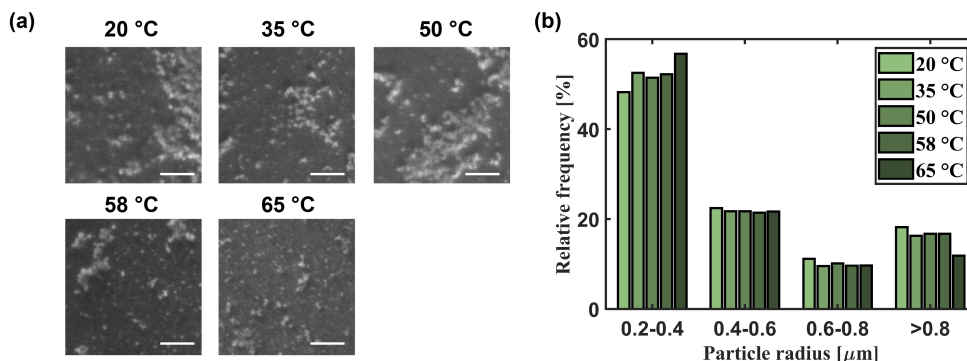


Figure 12. (a) TIRF images of asphaltene particles at the final state of different temperatures. The length of the scale bar is 5 μm . (b) Relative frequency of size distribution of asphaltene particles at different temperatures.

by these ‘soluble-like’ asphaltene do not form aggregates but exist as PSMPs on the substrate to cause a higher R_p .

4. Conclusions

Dilution-induced asphaltene precipitation was experimentally investigated using a solvent exchange method in a microchamber. The size distribution of asphaltene precipitates in high resolution images was analyzed and compared after 20 different mixing conditions with a paraffinic solvent, including flow rate, chamber height and orientation, and the solvent temperature. In the same microfluidic chamber, increasing the flow rate of paraffinic solvents accelerated the aggregation rate but caused the particle growth to stop at smaller levels. However, the flow rate had no obvious effect on the surface coverage of asphaltene precipitates. The surface coverage and size of asphaltene precipitates increased with the chamber height, regardless of the orientation of the chamber. But both the surface coverage and size of asphaltene particles of the horizontally placed device were larger than the vertically placed device when the channel height was higher than 180 μm . The difference between a horizontally and a vertically chamber was attributed the for-

mation of convective rolls caused by gravity, which vanished in a narrow chamber ($90\ \mu\text{m}$ in height). Moreover, our results showed that higher temperatures resulted in lower SC and larger particle sizes from 20 to $65\ ^\circ\text{C}$, possibly due to more stable asphaltene in the mixture liquid at higher temperature. For all mixing conditions, the oversaturation pulse resulted from the solvent exchange process were simulated using a finite element method based multiphysics solver. Our model results corroborated well with the experimental results. The combination of the experimental and simulation results demonstrated the significance of mixing dynamics on the morphology of the asphaltene precipitates.

The important implication from this study is that mixing conditions, such as flow rate, temperature, orientation, and dimension of microchamber, may be potentially leveraged as a cost-saving and effective approach to controlled asphaltene precipitation without using additional paraffinic solvents. Our work covers a wide range of mixing conditions to be relevant to many situations. Furthermore, this implication is not only applicable to asphaltene precipitation, but to other dilution-induced phase separation processes, such as nanoparticle aggregation or polymer precipitation.

Declaration of Competing Interests

The authors declare that they have no known competing financial interests or personal relationships that could have appeared to influence the work reported in this paper.

Acknowledgement

The authors acknowledge the funding support from the Institute for Oil Sands Innovation (IOSI) (project number IOSI 2018-03), from the Natural Science and Engineering Research Council of Canada (NSERC)-Collaborative Research and Development Grants, and from the Canada Research Chair Program and from Canada Foundation for Innovation, John R. Evans Leaders Fund. The authors are grateful for technical support from IOSI lab, particularly from Lisa Brandt and Brittany MacKinnon. We also thank Compute Canada (www.computecanada.ca) for the computational facility and technical

support. We are also grateful to Gilmar F. Arends for his help on symmetry software, Dr. Shantanu Maheshwari for his help on COMSOL simulations, and our industry steward Dr. Sepideh Mortazavi Manesh for the fruitful discussion.

Nomenclature

- $\alpha_{i,j}$ = Collision frequency ($m^3/mol \cdot s$)
 $\beta_{i,j}$ = Collision efficiency
 δ = Hildebrand solubility parameter ($MPa^{1/2}$)
 C = Concentration (mol/L)
 d = Diameter of particle (μm)
 D = Diffusion coefficient (m^2/s)
 F = Interfacial tension (N/m)
 g = Gravitational constant (m/s^2)
 G = Shear force (s^{-1})
 h = Channel height (μm)
 J = Mass flux ($kg/m^2 \cdot s$)
 k_B = Boltzmann constant (J/K)
 $K_{i,j}$ = Aggregation kernel
 K_m = Correction for discontinuity of fluid
 μ = Viscosity ($mPa \cdot s$)
 ν = Kinematic viscosity (m^2/s)
 n = quantity of particle
 N = Avogadro constant (mol^{-1})
 N_{psmp} = Quantity of primary submicron particles
 N_{smp} = Quantity of submicron particles
 ϕ = Level-Set function
 P = Pressure (Pa)
 Pe = Péclet number

Q = Flow rate (m^3/s)
 ρ = Density (kg/m^3)
 R = Ideal gas constant ($J/K \cdot mol$)
 Ra = Rayleigh number
 Re = Reynolds number
 R_p = Ratio of primary submicron particles (%)
 t = Time (s)
 T = Temperature (K)
 U = Mass average velocity (kg/s)
 w = Width (μm)
 \bar{X} = Particle moving distance (m)

References

- [1] M. R. Gray, Upgrading oilsands bitumen and heavy oil, University of Alberta, 2015.
- [2] B. Schuler, G. Meyer, D. Peña, O. C. Mullins, L. Gross, Unraveling the molecular structures of asphaltenes by atomic force microscopy, *J. Am. Chem. Soc.* 137 (31) (2015) 9870–9876.
- [3] X. Mao, L. Gong, L. Xie, H. Qian, X. Wang, H. Zeng, Novel Fe_3O_4 based superhydrophilic core-shell microspheres for breaking asphaltenes-stabilized water-in-oil emulsion, *Chem. Eng. J.* 358 (2019) 869–877.
- [4] J. Ma, X. Li, X. Zhang, H. Sui, L. He, S. Wang, A novel oxygen-containing demulsifier for efficient breaking of water-in-oil emulsions, *Chem. Eng. J.* 385 (2020) 123826.
- [5] K. Keshmiri, H. Huang, N. Nazemifard, Microfluidic platform to evaluate asphaltene deposition during solvent-based extraction of bitumen, *Fuel* 239 (2019) 841–851.
- [6] M. Zi, G. Wu, J. Wang, D. Chen, Investigation of gas hydrate formation and inhibition in oil-water system containing model asphaltene, *Chem. Eng. J.* 412 (2021) 128452.
- [7] F. Rao, Q. Liu, Froth treatment in athabasca oil sands bitumen recovery process: A review, *Energy Fuels* 27 (12) (2013) 7199–7207.
- [8] M. Plata-Gryl, M. Momotko, S. Makowiec, G. Boczka, Characterization of diatomaceous earth coated with nitrated asphaltenes as superior adsorbent for removal of vocs from gas phase in fixed bed column, *Chem. Eng. J.* 427 (2022) 130653.
- [9] N. H. M. H. Tehrani, M. S. Alivand, D. M. Maklavany, A. Rashidi, M. Samipoorgiri, A. Seif,

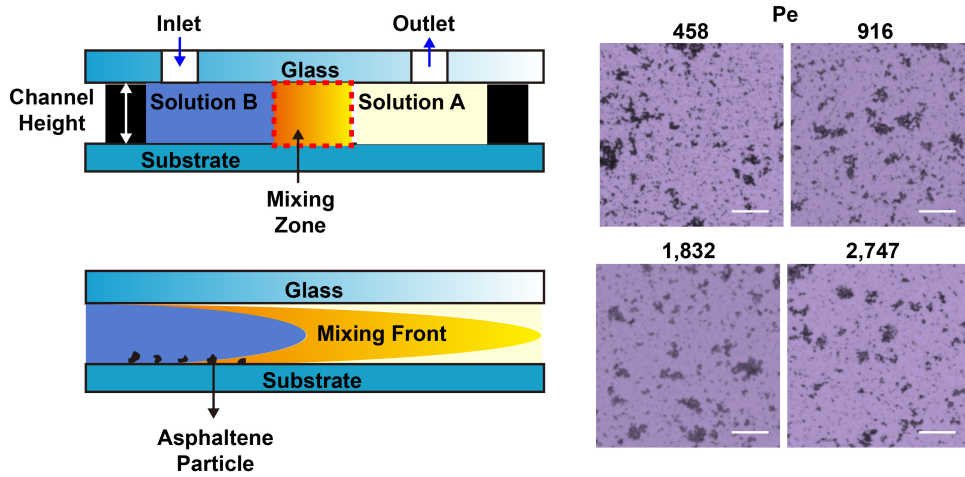
- Z. Yousefian, Novel asphaltene-derived nanoporous carbon with ns-rich micro-mesoporous structure for superior gas adsorption: Experimental and dft study, *Chem. Eng. J.* 358 (2019) 1126–1138.
- [10] M. S. Alivand, M. Najmi, N. H. M. H. Tehrani, A. Kamali, O. Tavakoli, A. Rashidi, M. D. Esrafil, E. Ghasemy, O. Mazaheri, Tuning the surface chemistry and porosity of waste-derived nanoporous materials toward exceptional performance in antibiotic adsorption: Experimental and dft studies, *Chem. Eng. J.* 374 (2019) 274–291.
- [11] S. Saad, A. S. Zeraati, S. Roy, M. A. S. R. Saadi, J. R. Radović, A. Rajeev, K. A. Miller, S. Bhattacharyya, S. R. Larter, G. Natale, et al., Transformation of petroleum asphaltenes to carbon fibers, *Carbon* (2022).
- [12] H. W. Yarranton, D. Ortiz, D. Barrera, E. Baydak, L. Barré, D. Frot, J. Eyssautier, H. Zeng, Z. Xu, G. Dechaine, et al., On the size distribution of self-associated asphaltenes, *Energy Fuels* 27 (9) (2013) 5083–5106.
- [13] O. C. Mullins, The modified yen model, *Energy Fuels* 24 (4) (2010) 2179–2207.
- [14] O. Elkhatib, W. Chaisoontornyotin, M. Gesho, L. Goual, Nanoscale investigation of asphaltene deposition under capillary flow conditions, *Energy Fuels* 34 (5) (2019) 5148–5158.
- [15] B. Zhao, J. M. Shaw, Composition and size distribution of coherent nanostructures in athabasca bitumen and maya crude oil, *Energy Fuels* 21 (5) (2007) 2795–2804.
- [16] J. Eyssautier, D. Espinat, J. Gummel, P. Levitz, M. Becerra, J. Shaw, L. Barré, Mesoscale organization in a physically separated vacuum residue: Comparison to asphaltenes in a simple solvent, *Energy Fuels* 26 (5) (2012) 2680–2687.
- [17] M. R. Gray, R. R. Tykwinski, J. M. Stryker, X. Tan, Supramolecular assembly model for aggregation of petroleum asphaltenes, *Energy Fuels* 25 (7) (2011) 3125–3134.
- [18] L. M. da Costa, S. R. Stoyanov, S. Gusarov, X. Tan, M. R. Gray, J. M. Stryker, R. Tykwinski, J. W. de M. Carneiro, P. R. Seidl, A. Kovalenko, Density functional theory investigation of the contributions of π - π stacking and hydrogen-bonding interactions to the aggregation of model asphaltene compounds, *Energy Fuels* 26 (5) (2012) 2727–2735.
- [19] S. Wang, J. Liu, L. Zhang, J. Masliyah, Z. Xu, Interaction forces between asphaltene surfaces in organic solvents, *Langmuir* 26 (1) (2010) 183–190.
- [20] S. Wang, J. Liu, L. Zhang, Z. Xu, J. Masliyah, Colloidal interactions between asphaltene surfaces in toluene, *Energy Fuels* 23 (2) (2009) 862–869.
- [21] S. Peramanu, P. F. Clarke, B. B. Pruden, Flow loop apparatus to study the effect of solvent, temperature and additives on asphaltene precipitation, *J. Pet. Sci. Eng.* 23 (2) (1999) 133–143.
- [22] K. Akbarzadeh, H. Alboudwarej, W. Y. Svrcek, H. W. Yarranton, A generalized regular solution model for asphaltene precipitation from n-alkane diluted heavy oils and bitumens, *Fluid Ph. Equilibria.* 232 (1-2) (2005) 159–170.

- [23] F. M. Alemi, S. Mohammadi, S. A. M. Dehghani, A. Rashidi, N. Hosseinpour, A. Seif, Experimental and dft studies on the effect of carbon nanoparticles on asphaltene precipitation and aggregation phenomena, *Chem. Eng. J.* 422 (2021) 130030.
- [24] E. Rogel, M. Moir, Effect of precipitation time and solvent power on asphaltene characteristics, *Fuel* 208 (2017) 271–280.
- [25] E. Hristova, P. Tchoukov, S. R. Stoyanov, R. McFarlane, Asphaltene precipitation onsets in relation to the critical dilution of athabasca bitumen in paraffinic solvents, *Energy Fuels* (2022).
- [26] H. Alboudwarej, K. Akbarzadeh, J. Beck, W. Y. Svrcek, H. W. Yarranton, Regular solution model for asphaltene precipitation from bitumens and solvents, *AIChE J.* 49 (11) (2003) 2948–2956.
- [27] N. H. Rahmani, J. H. Masliyah, T. Dabros, Characterization of asphaltenes aggregation and fragmentation in a shear field, *AIChE J.* 49 (7) (2003) 1645–1655.
- [28] N. H. Rahmani, T. Dabros, J. H. Masliyah, Evolution of asphaltene floc size distribution in organic solvents under shear, *Chem. Eng. Sci.* 59 (3) (2004) 685–697.
- [29] E. S. Boek, A. D. Wilson, J. T. Padding, T. F. Headen, J. P. Crawshaw, Multi-scale simulation and experimental studies of asphaltene aggregation and deposition in capillary flow, *Energy Fuels* 24 (4) (2010) 2361–2368.
- [30] E. S. Boek, H. K. Ladva, J. P. Crawshaw, J. T. Padding, Deposition of colloidal asphaltene in capillary flow: Experiments and mesoscopic simulation, *Energy Fuels* 22 (2) (2008) 805–813.
- [31] M. Ali, M. Islam, The effect of asphaltene precipitation on carbonate-rock permeability: an experimental and numerical approach, *SPE Prod. Faci.* 13 (03) (1998) 178–183.
- [32] N. H. Rahmani, T. Dabros, J. H. Masliyah, Online optical monitoring of asphaltene aggregation, *Ind. Eng. Chem. Res.* 44 (1) (2005) 75–84.
- [33] K. Rastegari, W. Y. Svrcek, H. W. Yarranton, Kinetics of asphaltene flocculation, *Ind. Eng. Chem. Res.* 43 (21) (2004) 6861–6870.
- [34] D. D. Nguyen, R. Daneshfar, A. H. S. Dehaghani, C.-H. Su, The effect of shear rate on aggregation and breakage of asphaltene flocs: experimental study and model-based analysis, *J. Mol. Liq.* 325 (2021) 114861.
- [35] A. S. Shalygin, I. V. Kozhevnikov, S. G. Kazarian, O. N. Martyanov, Spectroscopic imaging of deposition of asphaltene from crude oil under flow, *J. Pet. Sci. Eng.* 181 (2019) 106205.
- [36] E. V. Morozov, O. N. Martyanov, Reversibility of asphaltene aggregation as revealed by magnetic resonance imaging in situ, *Energy Fuels* 31 (10) (2017) 10639–10647.
- [37] J. S. Buckley, T. Fan, Z. Tong, N. R. Morrow, Mixing small amounts of crude oil with large amounts of asphaltene precipitant, in: *Proceedings of the International Society of Core Analysts Symposium*, Citeseer, 2006, pp. 1–12.
- [38] E. Durand, M. Clemancey, J.-M. Lancelin, J. Verstraete, D. Espinat, A.-A. Quoineaud, Effect of

- chemical composition on asphaltene aggregation, *Energy Fuels* 24 (2) (2010) 1051–1062.
- [39] S. Mozaffari, H. Ghasemi, P. Tchoukov, J. Czarnecki, N. Nazemifard, Lab-on-a-chip systems in asphaltene characterization: a review of recent advances, *Energy Fuels* 35 (11) (2021) 9080–9101.
- [40] N. M. Pagán Pagán, Z. Zhang, T. V. Nguyen, A. B. Marciel, S. L. Biswal, Physicochemical characterization of asphaltene using microfluidic analysis, *Chem. Rev.* (2022).
- [41] J. Meng, J. B. You, H. Hao, X. Tan, X. Zhang, Primary submicron particles from early stage asphaltene precipitation revealed in situ by total internal reflection fluorescence microscopy in a model oil system, *Fuel* 296 (2021) 120584.
- [42] J. Meng, J. B. You, G. F. Arends, H. Hao, X. Tan, X. Zhang, Microfluidic device coupled with total internal reflection microscopy for in situ observation of precipitation, *Eur. Phys. J. E* 44 (4) (2021) 1–8.
- [43] J. Meng, S. G. Sontti, M. Sadeghi, G. F. Arends, P. Nikrityuk, X. Tan, X. Zhang, Size distribution of primary submicron particles and larger aggregates in solvent-induced asphaltene precipitation in a model oil system, *Fuel* 322 (2022) 124057.
- [44] X. Zhang, Z. Lu, H. Tan, L. Bao, Y. He, C. Sun, D. Lohse, Formation of surface nanodroplets under controlled flow conditions, *Proc. Natl. Acad. Sci.* 112 (30) (2015) 9253–9257.
- [45] S. Peng, V. Spandan, R. Verzicco, D. Lohse, X. Zhang, Growth dynamics of microbubbles on microcavity arrays by solvent exchange: Experiments and numerical simulations, *J. Colloid Interface Sci.* 532 (2018) 103–111.
- [46] J. Meng, J. B. You, X. Zhang, Viscosity-mediated growth and coalescence of surface nanodroplets, *J. Phys. Chem.* 124 (23) (2020) 12476–12484.
- [47] X. Zhang, Z. Wei, H. Choi, H. Hao, H. Yang, Oiling-out crystallization of beta-alanine on solid surfaces controlled by solvent exchange, *Adv. Mater. Interfaces* 8 (2) (2021) 2001200.
- [48] H. Choi, Z. Wei, J. B. You, H. Yang, X. Zhang, Effects of chemical and geometric microstructures on the crystallization of surface droplets during solvent exchange, *Langmuir* 37 (17) (2021) 5290–5298.
- [49] C. Zhang, V. J. Pansare, R. K. Prud’Homme, R. D. Priestley, Flash nanoprecipitation of polystyrene nanoparticles, *Soft Matter* 8 (1) (2012) 86–93.
- [50] B. Dyett, A. Kiyama, M. Rump, Y. Tagawa, D. Lohse, X. Zhang, Growth dynamics of surface nanodroplets during solvent exchange at varying flow rates, *Soft matter* 14 (25) (2018) 5197–5204.
- [51] J. Meng, J. B. You, H. Hao, X. Tan, X. Zhang, Primary submicron particles from early stage asphaltene precipitation revealed in situ by total internal reflection fluorescence microscopy in a model oil system, *Fuel* 296 (2021) 120584.
- [52] M. Sussman, P. Smereka, S. Osher, A level set approach for computing solutions to incompressible two-phase flow, *J. Comput. Phys.* 114 (1) (1994) 146–159.
- [53] J. O. McCaslin, O. Desjardins, A localized re-initialization equation for the conservative level set

- method, *J. Comput. Phys.* 262 (2014) 408–426.
- [54] COMSOL Multiphysics[®] User Guide, v. 6.0. (2021).
- [55] Schlumberger, VMG Symmetry, v2021.2 (2021).
URL <https://www.software.slb.com/products/symmetry>
- [56] H. Yu, S. Maheshwari, J. Zhu, D. Lohse, X. Zhang, Formation of surface nanodroplets facing a structured microchannel wall, *Lab Chip*. 17 (2017) 1496–1504.
- [57] Z. Wei, J. B. You, H. Zeng, X. Zhang, Interfacial partitioning enhances microextraction by multi-component nanodroplets, *J. Phys. Chem.* 126 (3) (2022) 1326–1336.
- [58] T. Maqbool, S. Raha, M. P. Hoepfner, H. S. Fogler, Modeling the aggregation of asphaltene nanoaggregates in crude oil- precipitant systems, *Energy Fuels* 25 (4) (2011) 1585–1596.
- [59] N. N. Nassar, S. Betancur, S. Acevedo, C. A. Franco, F. B. Cortés, Development of a population balance model to describe the influence of shear and nanoparticles on the aggregation and fragmentation of asphaltene aggregates, *Ind. Eng. Chem. Res.* 54 (33) (2015) 8201–8211.
- [60] A. R. Solaimany-Nazar, H. Rahimi, Dynamic determination of asphaltene aggregate size distribution in shear induced organic solvents, *Energy Fuels* 22 (5) (2008) 3435–3442.
- [61] D. Thomas, S. Judd, N. Fawcett, Flocculation modelling: a review, *Water Res.* 33 (7) (1999) 1579–1592.
- [62] D. S. Parker, W. J. Kaufman, D. Jenkins, Floc breakup in turbulent flocculation processes, *J. Sanit. Eng. Div.* 98 (1) (1972) 79–99.
- [63] P. Kapur, Self-preserving size spectra of comminuted particles, *Chem. Eng. Sci.* 27 (2) (1972) 425–431.
- [64] J. D. Boadway, Dynamics of growth and breakage of alum floc in presence of fluid shear, *J. Env. Eng. Div. Proc.* 104 (5) (1978) 901–915.
- [65] J. Pandya, L. Spielman, Floc breakage in agitated suspensions: theory and data processing strategy, *J. Colloid Interface Sci.* 90 (2) (1982) 517–531.
- [66] Y. Xu, Asphaltene precipitation in paraffinic froth treatment: effects of solvent and temperature, *Energy Fuels* 32 (3) (2017) 2801–2810.
- [67] T. Allen, Particle size measurement, Springer, 1990.
- [68] S. Acevedo, A. Castro, E. Vasquez, F. Marcano, M. A. Ranaudo, Investigation of physical chemistry properties of asphaltenes using solubility parameters of asphaltenes and their fractions a1 and a2, *Energy Fuels* 24 (11) (2010) 5921–5933.
- [69] Z. Yang, S. Chen, H. Peng, M. Li, M. Lin, Z. Dong, J. Zhang, Y. Ji, Effect of precipitating environment on asphaltene precipitation: precipitant, concentration, and temperature, *Colloids Surf. A Physicochem. Eng. Asp.* 497 (2016) 327–335.

Graphical abstract



Highlights

- Analyze asphaltene precipitates > 200 nm from mixing a model oil with heptane
- Simulate mixing dynamics by a validated multiphysics model
- Reveal significance of mixing conditions in asphaltene precipitation
- Local concentration and shear forces impact size and amount of the precipitates
- Primary submicron particles form universally under all 20 mixing conditions